HHS Public Access

Author manuscript

*Nat Mater*. Author manuscript; available in PMC 2015 August 17.

Published in final edited form as:

*Nat Mater*. 2015 May ; 14(5): 532–539. doi:10.1038/nmat4249.

# Biodegradable silicon nanoneedles delivering nucleic acids intracellularly induce localized *in vivo* neovascularization

**C. Chiappini**[1,2,†], **E. De Rosa**[3,†], **J. O. Martinez**[3], **X. Liu**[3], **J. Steele**[1,2], **M. M. Stevens**[1,2,*], and **E. Tasciotti**[3,*]

[1]Department of Materials, Imperial College London, London SW6 7PB, UK

[2]Department of Bioengineering and Institute of Biomedical Engineering, Imperial College London, London SW6 7PB, UK

[3]Department of Nanomedicine, Houston Methodist Research Institute, Houston, Texas 77030, USA

## Abstract

The controlled delivery of nucleic acids to selected tissues remains an inefficient process mired by low transfection efficacy, poor scalability because of varying efficiency with cell type and location, and questionable safety as a result of toxicity issues arising from the typical materials and procedures employed. High efficiency and minimal toxicity *in vitro* has been shown for intracellular delivery of nuclei acids by using nanoneedles, yet extending these characteristics to *in vivo* delivery has been difficult, as current interfacing strategies rely on complex equipment or active cell internalization through prolonged interfacing. Here, we show that a tunable array of biodegradable nanoneedles fabricated by metal-assisted chemical etching of silicon can access the cytosol to co-deliver DNA and siRNA with an efficiency greater than 90%, and that *in vivo* the nanoneedles transfect the VEGF-165 gene, inducing sustained neovascularization and a localized sixfold increase in blood perfusion in a target region of the muscle.

The efficacy of protein and peptide therapy on biological processes[1,2] and the ability of nucleic acid to modulate gene expression[3] has fuelled a renewed interest in the delivery of



*Correspondence and requests for materials should be addressed to M.M.S. or E.T. m.stevens@imperial.ac.uk; etasciotti@houstonmethodist.org.

†These authors contributed equally to this work.

**Author contributions**

C.C., E.T. and M.M.S. designed the research. C.C. and E.T. conceived the nanoneedles; C.C. developed the nanoneedles with contributions from X.L.; C.C. evaluated loading, release, delivery and efficacy with contributions from E.D.R.; C.C. imaged biodegradation and cell interaction with contributions from E.D.R.; C.C. wrote the initial manuscript with contributions from E.D.R. and J.O.M. C.C. performed all electron microscopy analysis. E.D.R. and J.O.M. assessed cytocompatibility; E.D.R. designed and performed animal surgeries, intravital imaging and quantification of vascularization, vasculature pattern, and extravasation and flow rate over time on VEGF treatment, with contributions from J.O.M. J.O.M. evaluated degradation by ICP-AES, fluorescent and bioluminescent imaging and analysis, real-time PCR, and histological evaluation and staining of tissues with contributions from E.D.R. J.S. performed compressive mechanical testing. E.T. and M.M.S. contributed equally to the work, with M.M.S. supervising the *in vitro* studies and E.T. the *in vivo* work. All authors discussed and commented on the manuscript.

Supplementary information is available in the online version of the paper.

**Competing financial interests**

The authors declare no competing financial interests.

biological therapeutics for the study of tissue function. In particular, the localized transfer of genetic material to temporarily alter tissue structure and function in a desired spatial pattern may enable the study of biologically initiated processes in the context of live adult tissues[4]. Nucleic acids act on intracellular targets and must localize in an active form to either the cytosol or the nucleus to be effective. Being large charged molecules, they cannot easily cross the plasma membrane unless actively ferried[5]. Inefficient transfection[5–7], safety concerns[8,9], limited site accessibility[10] and poor scalability[11] still hamper the *in vivo* delivery of nucleic acids. Nanoneedles can efficiently transfer bioactive agents to many cells in parallel[12], sense their electrical activity[13], or transduce optical information from within the cytoplasm[14] with minimal impact on viability[15] and metabolism[16]. The mechanism for nanoneedle-mediated cytosolic delivery is still highly debated; conflicting evidence supports either cytosolic display of the nanoneedles[12,17] or cell permeabilization due to membrane deformation[18,19].Nanoneedles at present rely on active cell processes[17,20] or complex equipment for payload delivery[21,22], limiting their use *in vivo*.

We hypothesized that *in vivo* patterning of gene expression could be mediated by the intracellular delivery of nucleic acids through their injection by vertical arrays of biodegradable porous nanoneedles.

## Characterization of porous silicon nanoneedles

Porous silicon is a biodegradable[23,24] material amenable to microfabrication[25],with favourable toxicology and versatile delivery properties[26,27] for systemic[27,28] and intra-organ[29] administration as well as for the manufacturing of implantable devices[30]. The nanoneedles were fabricated by combining metal-assisted chemical etch[31] with standard microfabrication (Fig. 1a–c). Their geometry was tailored to optimize the fundamental parameters necessary for intracellular delivery, including mechanical stability, cell-membrane penetration, cytotoxicity and loading capacity (pore volume). The tunable tip diameter was reduced to less than 50 nm, amply below the cutoff diameter established for nanoneedle cytotoxicity[32] (Fig. 1c). The prototypical porous conical nanoneedle had 5 μm length, 50nm apical width and 600nm base diameter (Fig. 1b), providing an over 300-fold increase in surface area for payload adsorption compared to a solid cylindrical nanowire of equivalent apical diameter ($2.4 \times 10^8$ versus $7.8 \times 10^5$ $nm^2$). The needles' porosity could be tailored between 45% and 70%, allowing the modulation of degradation time, payload volume and mechanical properties[31]. Conical nanoneedles were extremely robust, as confirmed by their structural integrity following *in vitro* and *in vivo* applications (Supplementary Fig. 1). A failure load of 260 nN and a critical buckling load of 264 nN were estimated for the nanoneedles; two orders of magnitude higher than the forces experienced during active penetration of a cell (0.5 to 2 nN; ref. 32; Supplementary Information). Compression testing highlighted the onset of nanoneedle failure at 3.1 μN, with terminal failure occurring at 6.2 μN (Supplementary Fig. 2).

Nanoneedles progressively dissolved over time in physiologic conditions (Fig. 1d,e), first thinning and increasing in porosity, and ultimately losing their shape after 15 h. By 72 h only their solid stump remained. The atomic quantification of Si released in solution confirmed the progressive degradation of the nanoneedles, which was substantially achieved

within 36 h (Fig. 1e). This unique degradation behaviour, not exhibited by solid nanoneedles, enables our system to temporarily interface with cells, and to completely dissolve over time.

## Gene regulation by nanoinjection of nucleic acids

Cells were interfaced with nanoneedles (that is, nanoinjected) either by seeding them over the nanoneedles (needles on bottom, nN-B) or by pressing the nanoneedles over a monolayer of cells (needles on top, nN-T). Although the nN-B setting was crucial to understand the cell–nanoneedle interface, nN-T better mimicked the *in vivo* delivery setting. When cells were seeded over the nanoneedles, they appeared to interface with the cell membrane within 4 h (Fig. 2a), whereas the nN-T strategy yielded immediate interfacing (Fig. 2b). Under either condition the cells retained physiologic metabolic activity and normal proliferation over the course of five days (Fig. 2c). Furthermore, nanoinjection did not induce significant toxicity. According to the lactate dehydrogenase (LDH) assay, the concentration of the enzyme in the culture medium was unaltered by the needles, suggesting that nanoinjection did not induce the leakage of intracellular material (Fig. 2d).

Nanoneedles efficiently loaded and retained nucleic acids, releasing them over 12–18 h (Supplementary Figs 3 and 4). Both nanoinjection strategies delivered nucleic acids intracellularly and were able to regulate gene expression. After 30 min of nN-B nanoinjection, siRNA delivery to cells was minimal. However, at 24 h and 48 h, siRNA was uniformly distributed throughout the cytosol (Fig. 3a and Supplementary Fig. 5). In the nN-T setting, nanoneedles were applied onto cells using a 100 relative centrifugal force (rcf) acceleration, and left in place for 30 min to deliver the siRNA to the cytosol (Supplementary Fig. 5). Nanoinjection required either cellular activity or application of an external force. When cellular activity was impaired by maintaining the culture at 4 °C, nN-T nanoinjection at 0 rcf did not yield any cytosolic delivery over 4 h (Supplementary Fig. 6). In contrast, forceful nanoinjection at 4 °C and 100 rcf yielded cytosolic delivery of siRNA.

The co-loading of a Cy3-labelled siRNA and a GFP-expressing DNA plasmid proved the nanoneedles' ability to co-deliver two types of nucleic acids to the same cell (Fig. 3). The transfection of active nucleic acids into HeLa cells was determined by assessing GFP expression and measuring siRNA fluorescence within nanoinjected cells (Fig. 3a–c). Transfection efficiency was greater than 90% at 48 h (Fig. 3b,c and Supplementary Fig. 7). Green fluorescence was present at 48 h surrounding the stumps of nanoneedles loaded with Cy3–siRNA (Fig. 3a). This signal could arise from the GFP originating either from the cell cytosol[33] or from microvesicles in solution[34–36], and adsorbed in the mesoporous silicon matrix[37]. The effect of glyceraldehyde-3-phosphate-dehydrogenase (GAPDH) siRNA nanoinjection was confirmed by the 80% ($p < 0.001$) silencing in GAPDH expression compared to controls and to cells nanoinjected with scrambled siRNA (Fig. 3d,e). No silencing was observed for nanoinjection with empty needles in the presence of GAPDH siRNA in solution, supporting the hypothesis of nanoneedle-mediated, direct delivery of the payload in the cell cytoplasm.

## Localized nanoinjection to tissue

We optimized nanoinjection *in vivo* by applying nanoneedles loaded with fluorescent dyes to the skin and muscle of test mice. All *in vivo* studies employed nanoneedles with 50-nm-diameter tips and a 2 μm pitch. Eighty per cent of the loaded dye was transferred into an area of the skin replicating the chip's size and shape. The concentration and localization of the dye was maintained for up to 48 h, even after washing (Fig. 4a,b), and remained close to the surface (localized patterning; Supplementary Fig. 8). In contrast, topical application or delivery through a flat chip showed a limited retention and a patchy distribution of the dye across the tissue (Fig. 4c and Supplementary Fig. 9). Unlike microneedles that show a gradient of effect originating from each puncture site[38], nanoinjection provided a more uniform delivery owing to the high density of nanoneedles per surface area (Fig. 4d). Nanoinjection to the ear and to the muscle demonstrated similar uniformity, localization and retention patterns (Fig. 4b and Supplementary Fig. 9). These findings confirmed the ability of the nanoneedles to confine the treatment to a localized region, regardless of tissue architecture, stiffness and degree of vascularization.

## Safety of nanoinjection *in vivo*

To evaluate *in vivo* safety, we assessed the impact of nanoinjection with empty nanoneedles on different murine tissues at the micro- and nanoscale. Real-time bioluminescent imaging following administration of luminol[39] showed that nanoinjection did not induce local acute inflammation in muscle or skin at 5 and 24 h (Fig. 5a,b).

The impact at the site of interfacing was assessed in muscle, skin and ear tissues. Haematoxylin and eosin (H&E) histology and electron microscopy analysis indicated substantial similarity between untreated and nanoinjected tissues. The local myofibres showed normalmorphology with minimal disintegration or leukocyte infiltration (Fig. 5c and Supplementary Fig. 10a). The histological analysis showed intact tissue membranes after nanoinjection. Treated skin showed preserved epidermis, dermis, and sebaceous-gland and hair-follicle layers typical of nude mice, with no sign of leukocyte infiltration (Fig. 5c). The skin showed no signs of epidermal, dermal or capillary vessel disruption, with normal keratinocyte levels and minimal thickening of the epidermis as well as negligible signs of hyperkeratosis or necrotic keratinocytes.

Histological analysis also indicated the impact of nanoinjection on the overall structure of muscle at 5 h, 5 days and 15 days following treatment. At each time period the transverse and longitudinal sections revealed myofibres of uniform size and shape analogous to WT muscle. The area, mean diameter and roughness of individual myofibres were not significantly different from WT (Fig. 5d,e). The nuclei were located on the periphery, a feature characteristic of skeletal muscle cells (Fig. 5c and Supplementary Fig. 10b). H&E histology confirmed the absence of infiltrating cells, disintegrating or necrotic myofibres, or scar formation due to the treatment[40]. TEM histology of muscle revealed a preserved cellular ultrastructure (Fig. 5f,g). The muscles exhibited the conventional sarcomere structures (A-band, I-band, Z-line and M-line) with transversely aligned Z-lines within each myofibril. High magnification of the myofibrils, sarcoplasmic reticulum, mitochondria and

transverse tubules confirmed that the basic units and organelles of the muscles retained a physiologic morphology.

## Neovascularization by nanoinjection of VEGF plasmid

We compared the efficiency of nanoinjection of 100 μg of human VEGF165 plasmid DNA (pVEGF165) to the direct injection of the same amount of naked plasmid into the muscles of mice (Fig. 6). VEGF is a master angiogenic gene, which induces tissue neovascularization, increases vessel interconnectivity, perfusion, local vascular leakiness, and infiltration of circulating cells[41,42]. Real-time PCR analysis indicated that both treatments induced expression of human VEGF165 for up to seven days, with nanoinjection exhibiting an average higher expression than direct injection (Supplementary Fig. 11). In both instances, treated muscles progressively exhibited higher vascularization compared with the control over the course of two weeks (Fig. 6a). However, only the neovascularization induced by the nanoinjection demonstrated a surge in perfusion (Fig. 6b). Also, the neovasculature in nanoinjected muscles exhibited highly interconnected and structured vessels in proximity to the surface (Fig. 6a and Supplementary Figs 12–14), and a sixfold increase in overall blood perfusion (Fig. 6b) and in the number of nodes at 14 days (Fig. 6c). On the other hand, the direct injection did not result in significantly higher perfusion or an increase in number of nodes (Fig. 6b,c) compared to sham surgery. The moderate increase in perfusion observed in the control was due to the surgical treatment, which required a small incision of the fascia to expose the muscle. In this case, the increased perfusion was not associated with an increase in the number of nodes or with the formation of the irregular neovasculature as observed with nanoinjection (Fig. 6a–c), but to the physiologic increased blood flow to the area.

The new blood vessels formed after VEGF nanoinjection were functional, and had blood flow rates comparable to pre-existing vessels of similar size (Supplementary Movies 1–3 and Supplementary Figs 15 and 16). The vasculature of treated muscles revealed increased blood pooling, exhibiting both a greater number of pools and a larger total pool size at 7 and 14 days (Supplementary Fig. 14). This increased blood pooling indicates the formation of immature, leaky capillaries, as expected in response to VEGF expression[41]. Taken together, the data show that the nanoinjection of VEGF modulated the local gene expression, favouring tissue neovascularization and increased local blood perfusion.

## Outlook

We presented the synthesis and biomechanical characterization of porous silicon nanoneedles. The needles were biocompatible, biodegradable and could efficiently load and release nucleic acids directly in the cytosol, negotiating local biological barriers (for example, the cell membrane or the endolysosomal system). The nanoinjection of different nucleic acids could simultaneously up- or downregulate the expression of genes within a cell population confined in a region, thus enabling *in vivo* cell reprogramming within selected areas of a tissue. We demonstrated as a proof of concept that the nanoneedles mediated the *in situ* delivery of an angiogenic gene and triggered the patterned formation of new blood vessels. This paves the way for the *in vivo*, local control of the physiologic and structural features of a defined area of a tissue of interest.

The development of degradable nanoneedles highlights the transition towards biodegradable micro- and nano structures able to improve localized delivery while mitigating inflammation[43]. Microneedles are effective for three-dimensional delivery of payloads throughout tissues across hundreds of micrometres, and consequently their ability to target only a superficial layer of cells is greatly impaired[44]. Moreover, owing to the cell damage caused by their size, they induce local injury to the tissue, localized necrosis[45], and generate responses at the tissue and systemic level (transient immune activation)[43]. Conversely, nanoneedles are designed for extremely localized delivery to a few superficial layers of cells (two-dimensional patterning). This confined intracellular delivery has the potential to target specific exposed areas within a tissue, further reducing the invasiveness of the injection and limiting the impact on the overall structure of the tissue. The confined nature of nanoinjection at present requires only a small surgical incision to access non-exposed sites (for example, muscles). Furthermore, the nanoneedles can be applied to tissues with different structural and mechanical properties as a stepping stone towards the development of a non-immunogenic delivery platform for nucleic acids and other functional payloads to tissues.

The nanoinjection of the angiogenic master regulator gene, VEGF165, enabled minimally invasive, localized *in vivo* genetic engineering of the muscle tissue. This form of delivery ushers in countless possibilities to design and study the microarchitecture of tissues and highlights a strategy for microscale modulation of widely diverse biological processes, ranging from immune response to cell metabolism. In this study we focused on the induction of neoangiogenesis in the muscle tissue, because early vascularization is a key step in wound healing and scar-tissue remodelling. Moreover, the growth of a supporting blood-vessel network is crucial for the successful grafting of an implant. Most scaffolds employed in tissue engineering rely on the host's vasculature for the supply of oxygen and nutrients. The nanoneedles could be used to pre-condition the site of an implant by locally patterning a supplemental vascular network. This could support the early steps of tissue regeneration and, by enhancing the integration with the surrounding native tissue, increase the long-term performance of the implant[46].

## Methods

### Fabrication of the nanoneedles

Low-stress silicon nitride (160 nm) was deposited by low-pressure chemical vapour deposition over 100 mm, 0.01 Ω-cm, boron-doped p-type silicon wafers. A 600-nm-diameter disk array with desired pitch was patterned on the substrate by photolithography, and transferred into the silicon nitride layer by reactive ion etch in $CF_4$ plasma.

Following photoresist stripping, the substrate was cleaned in 10% HF for 60 s followed by deposition of Ag from 1mM $AgNO_3$ in 10% HF for 2 min. The substrate was rinsed in water and 2-propanol, and dried. Metal-assisted chemical etch of the substrate in 10% HF, 122mM $H_2O_2$ for 8 min 30 s formed porous silicon pillars with 600nm diameter and 9 μm height. The pillars were shaped into nanoneedles with apical diameter <50nm by reactive ion etch in $SF_6$ plasma. The substrate was cut into 8 × 8mm chips, and the nanoneedles on the chips were oxidized by $O_2$ plasma.

### Nanoinjection *in vitro*

8 × 8mm nanoneedle chips were sterilized in 70% ethanol for 1 h and allowed to dry under ultraviolet irradiation. nN-B: The chip was placed at the bottom of a 24-well plate, rinsed thrice with PBS, and $1 \times 10^5$ HeLa cells were seeded over the needles. The well plate was returned to the incubator. nN-T: HeLa cells were seeded at $5 \times 10^4$ cells in a 24-well plate and incubated for 24×48 h. Three ml of fresh medium were added, and the nanoneedle chip was immersed in medium face down. The plate spun at 100 rcf for 1 min in a swinging bucket centrifuge. For further culturing, the chip was removed from the well after 30 min of incubation, and placed face up in a new 24-well plate, with 0.5ml of fresh medium.

### Delivery of nucleic acids *in vitro*

The nanoneedles were functionalized with 3-aminopropyltriethoxysilane (APTES) by immersion for 2 h in 2% APTES in ethanol. GAPDH cy3–siRNA (50 μl, 100 nM) in PBS was spotted on the nanoneedles chip and incubated for 15 min, then rinsed three times with 100 μl of DI water. Nanoneedles were interfaced with cells either in the nN-T or nN-B settings. At 30 min and 24 h following treatment, cells were fixed, mounted on a coverslip, and analysed by confocal microscopy. GAPDH silencing was assayed by in-cell western at 24 h following nN-B treatment. GAPDH protein expression was quantified from the fluorescent intensity at 800nm normalized to the total chip surface area.

Alternatively, the chips were incubated with 20 μl of GAPDH cy3–siRNA (100 nM) and GFP plasmid (500 ng $\mu l^{-1}$) in PBS. The solution was allowed to dry over the nanoneedles, and the needles were immediately employed in a nN-B strategy. For confocal microscopy the cells were fixed at 48 h following transfection. For flow-cytometry analysis the cells were trypsinized, collected in a 1ml microcentrifuge tube, washed twice with PBS and then fixed.

### Nanoinjection *in vivo*

Animal studies were performed in accordance with the guidelines of the Animal Welfare Act and the Guide for the Care and Use of Laboratory Animals based on approved protocols by The University of Texas M.D. Anderson Cancer Center's (MDACC) and Houston Methodist Research Institute's (HMRI) Institutional Animal Care and Use Committees. Immediately before use, chips were cleaned, sterilized under ultraviolet light, and incubated with 20 μl of fluorescent dyes (1mg $ml^{-1}$) or pVEGF (5mg $ml^{-1}$) in PBS, which was allowed to dry.

Nanoneedles were pressed down using the thumb, ensuring minimal movement for at least 1 min, and then removed. For the muscle studies, a small incision was made on the upper-back right of the mouse before application.

Plasmid VEGF delivery was performed with a 1–2 cm dorsal midline incision to expose the superficial gluteal and lumbar muscles. VEGF-loaded pSi nanoneedles were implanted in direct contact with the lumbar and gluteal muscle on the right side, whereas the left side was left untreated. For the direct injection, 20 μl of VEGF (at 5mg $ml^{-1}$) were injected using a

Hamilton Neuros 25 μl syringe adjusted for a penetration depth of 200 μm to a similarly exposed muscle.

## Supplementary Material

Refer to Web version on PubMed Central for supplementary material.

## Acknowledgements

The authors would like to thank M. Giacca at the International Centre for Genetic Engineering and Biotechnology (ICGEB in Trieste, Italy) for kindly donating the pDNA-expressing VEGF-165, and I. K. Yazdi and R. Palomba for the amplification and purification of the plasmids used in the study. We are grateful to S. Amra for histology-slide preparation, D. Tinkey for surgical procedures, S. Zacchigna for suggestions on PCR protocols, P. Campagnolo for advice on SMA and isolectin staining, and S. T. Gammon for advice on bioluminescence imaging with luminol. This work was financially supported by: the US Department of Defense (W81XWH-12-10414) and the NIH (1R21CA173579-01A1 and 5U54CA143837); C.C. was supported by a Newton International Fellowship and a Marie Curie International Incoming Fellowship; J.O.M. was supported by a NIH pre-doctoral fellowship 5F31CA154119-02. M.M.S. holds an ERC grant ‘Naturale-CG’ and is supported by a Wellcome Trust Senior Investigator Award. E.T. holds grants from the Hearst Foundation and the Cullen Trust Foundation. C.C. and M.M.S. thank the Rosetrees Trust and the Stoneygate Trust for funding.

## References

1. Leader B, Baca QJ, Golan DE. Protein therapeutics: A summary and pharmacological classification. Nature Rev. Drug Discov. 2008; 7:21–39. [PubMed: 18097458]
2. Vlieghe P, Lisowski V, Martinez J, Khrestchatisky M. Synthetic therapeutic peptides: Science and market. Drug Discov. Today. 2010; 15:40–56. [PubMed: 19879957]
3. Kole R, Krainer AR, Altman S. RNA therapeutics: Beyond RNA interference and antisense oligonucleotides. Nature Rev. Drug Discov. 2012; 11:125–140. [PubMed: 22262036]
4. Khademhosseini A. Microscale technologies for tissue engineering and biology. Proc. Natl Acad. Sci. USA. 2006; 103:2480–2487. [PubMed: 16477028]
5. Whitehead KA, Langer R, Anderson DG. Knocking down barriers: Advances in siRNA delivery. Nature Rev. Drug Discov. 2009; 8:129–138. [PubMed: 19180106]
6. Saltzman WM, Luo D. Synthetic DNA delivery systems. Nature Biotechnol. 2000; 18:33–37. [PubMed: 10625387]
7. Thomas CE, Ehrhardt A, Kay MA. Progress and problems with the use of viral vectors for gene therapy. Nature Rev. Genet. 2003; 4:346–358. [PubMed: 12728277]
8. Mingozzi F, High KA. Therapeutic *in vivo* gene transfer for genetic disease using AAV: Progress and challenges. Nature Rev. Genet. 2011; 12:341–355. [PubMed: 21499295]
9. Lefesvre P, Attema J, van Bekkum D. A comparison of efficacy and toxicity between electroporation and adenoviral gene transfer. BMC Mol. Biol. 2002; 3:12. [PubMed: 12175426]
10. Aihara H, Miyazaki J-I. Gene transfer into muscle by electroporation *in vivo*. Nature Biotechnol. 1998; 16:867–870. [PubMed: 9743122]
11. Nishikawa M, Huang L. Nonviral vectors in the new millennium: Delivery barriers in gene transfe. Hum. Gene Ther. 2001; 12:861–870. [PubMed: 11387052]
12. Shalek AK, et al. Vertical silicon nanowires as a universal platform for delivering biomolecules into living cells. Proc. Natl Acad. Sci. USA. 2010; 107:1870–1875. [PubMed: 20080678]
13. Robinson JT, et al. Vertical nanowire electrode arrays as a scalable platform for intracellular interfacing to neuronal circuits. Nature Nanotech. 2012; 7:180–184.
14. Yan R, et al. Nanowire-based single-cell endoscopy. Nature Nanotech. 2011; 7:191–196.
15. Han SW, et al. High-efficiency DNA injection into a single human mesenchymal stem cell using a nanoneedle and atomic force microscopy. Nanomedicine: Nanotechnol. Biol. Med. 2008; 4:215–225.

16. Shalek AK, et al. Nanowire-mediated delivery enables functional interrogation of primary immune cells: Application to the analysis of chronic lymphocytic leukemia. Nano Lett. 2012; 12:6498–6504. [PubMed: 23190424]
17. Xu AM, et al. Quantification of nanowire penetration into living cells. Nature Commun. 2014; 5:3613. [PubMed: 24710350]
18. Sharei A, et al. A vector-free microfluidic platform for intracellular delivery. Proc. Natl Acad. Sci. USA. 2013; 110:2082–2087. [PubMed: 23341631]
19. Hanson L, Lin ZC, Xie C, Cui Y, Cui B. Characterization of the cell–nanopillar interface by transmission electron microscopy. Nano Lett. 2012; 12:5815–5820. [PubMed: 23030066]
20. Xie X, et al. Mechanical model of vertical nanowire cell penetration. Nano Lett. 2013; 13:6002–6008. [PubMed: 24237230]
21. Xie C, Lin Z, Hanson L, Cui Y, Cui B. Intracellular recording of action potentials by nanopillar electroporation. Nature Nanotech. 2012; 7:185–190.
22. Wang Y, et al. Poking cells for efficient vector-free intracellular delivery. Nature Commun. 2014; 5:4466. [PubMed: 25072981]
23. Anderson SHC, Elliott H, Wallis DJ, Canham LT, Powell JJ. Dissolution of different forms of partially porous silicon wafers under simulated physiological conditions. Phys. Status Solidi A. 2003; 197:331–335.
24. Canham LT. Bioactive silicon structure fabrication through nanoetching techniques. Adv. Mater. 1995; 7:1033–1037.
25. Chiappini C, et al. Tailored porous silicon microparticles: Fabrication and properties. Chem Phys Chem. 2010; 11:1029–1035. [PubMed: 20162656]
26. Tasciotti E, et al. Mesoporous silicon particles as a multistage delivery system for imaging and therapeutic applications. Nature Nanotech. 2008; 3:151–157.
27. Tanaka T, et al. Sustained small interfering RNA delivery by mesoporous silicon particles. Cancer Res. 2010; 70:3687–3696. [PubMed: 20430760]
28. Park J-H, et al. Biodegradable luminescent porous silicon nanoparticles for *in vivo* applications. Nature Mater. 2009; 8:331–336. [PubMed: 19234444]
29. Goh AS-W, et al. A novel approach to brachytherapy in hepatocellular carcinoma using a phosphorous32 (32P) brachytherapy delivery device—a first-in-man study. Int. J. Radiat. Oncol. Biol. Phys. 2007; 67:786–792. [PubMed: 17141975]
30. Anglin E, Cheng L, Freeman W, Sailor M. Porous silicon in drug delivery devices and materials. Adv. Drug Deliv. Rev. 2008; 60:1266–1277. [PubMed: 18508154]
31. Chiappini C, Liu X, Fakhoury JR, Ferrari M. Biodegradable porous silicon barcode nanowires with defined geometry. Adv. Funct. Mater. 2010; 20:2231–2239. [PubMed: 21057669]
32. Obataya I, Nakamura C, Han S, Nakamura N, Miyake J. Mechanical sensing of the penetration of various nanoneedles into a living cell using atomic force microscopy. Biosens. Bioelectron. 2005; 20:1652–1655. [PubMed: 15626623]
33. Na Y-R, et al. Probing enzymatic activity inside living cells using a nanowire–cell ‘sandwich’ assay. Nano Lett. 2013; 13:153–158. [PubMed: 23244056]
34. Muralidharan-Chari V, Clancy JW, Sedgwick A, D’Souza-Schorey C. Microvesicles: Mediators of extracellular communication during cancer progression. J. Cell Sci. 2010; 123:1603–1611. [PubMed: 20445011]
35. Ratajczak J, et al. Embryonic stem cell-derived microvesicles reprogram hematopoietic progenitors: Evidence for horizontal transfer of mRNA and protein delivery. Leukemia. 2006; 20:847–856. [PubMed: 16453000]
36. Yuan A, et al. Transfer of microRNAs by embryonic stem cell microvesicles. PLoS ONE. 2009; 4:e4722. [PubMed: 19266099]
37. Shen Z, et al. Porous silicon as a versatile platform for laser desorption/ionization mass spectrometry. Anal. Chem. 2000; 73:612–619. [PubMed: 11217770]
38. Lee JW, Park J-H, Prausnitz MR. Dissolving microneedles for transdermal drug delivery. Biomaterials. 2008; 29:2113–2124. [PubMed: 18261792]

39. Gross S, et al. Bioluminescence imaging of myeloperoxidase activity *in vivo*. Nature Med. 2009; 15:455–461. [PubMed: 19305414]

40. Luxembourg A, Evans CF, Hannaman D. Electroporation-based DNA immunisation: Translation to the clinic. Expert Opin. Biol. Ther. 2007; 7:1647–1664. [PubMed: 17961089]

41. Yancopoulos GD, et al. Vascular-specific growth factors and blood vessel formation. Nature. 2000; 407:242–248. [PubMed: 11001067]

42. Tammela T, Enholm B, Alitalo K, Paavonen K. The biology of vascular endothelial growth factors. Cardiovasc. Res. 2005; 65:550–563. [PubMed: 15664381]

43. DeMuth PC, et al. Polymer multilayer tattooing for enhanced DNA vaccination. Nature Mater. 2013; 12:367–376. [PubMed: 23353628]

44. Kim Y-C, Park J-H, Prausnitz MR. Microneedles for drug and vaccine delivery. Adv. Drug Deliv. Rev. 2012; 64:1547–1568. [PubMed: 22575858]

45. Gershonowitz A, Gat A. VoluDerm Microneedle Technology for Skin Treatments—*In Vivo* Histological Evidence. J. Cosmetic Laser Surg. 2015; 17:9–14.

46. Barrientos S, Stojadinovic O, Golinko MS, Brem H, Tomic-Canic M. Growth factors and cytokines in wound healing. Wound Repair Regen. 2008; 16:585–601. [PubMed: 19128254]

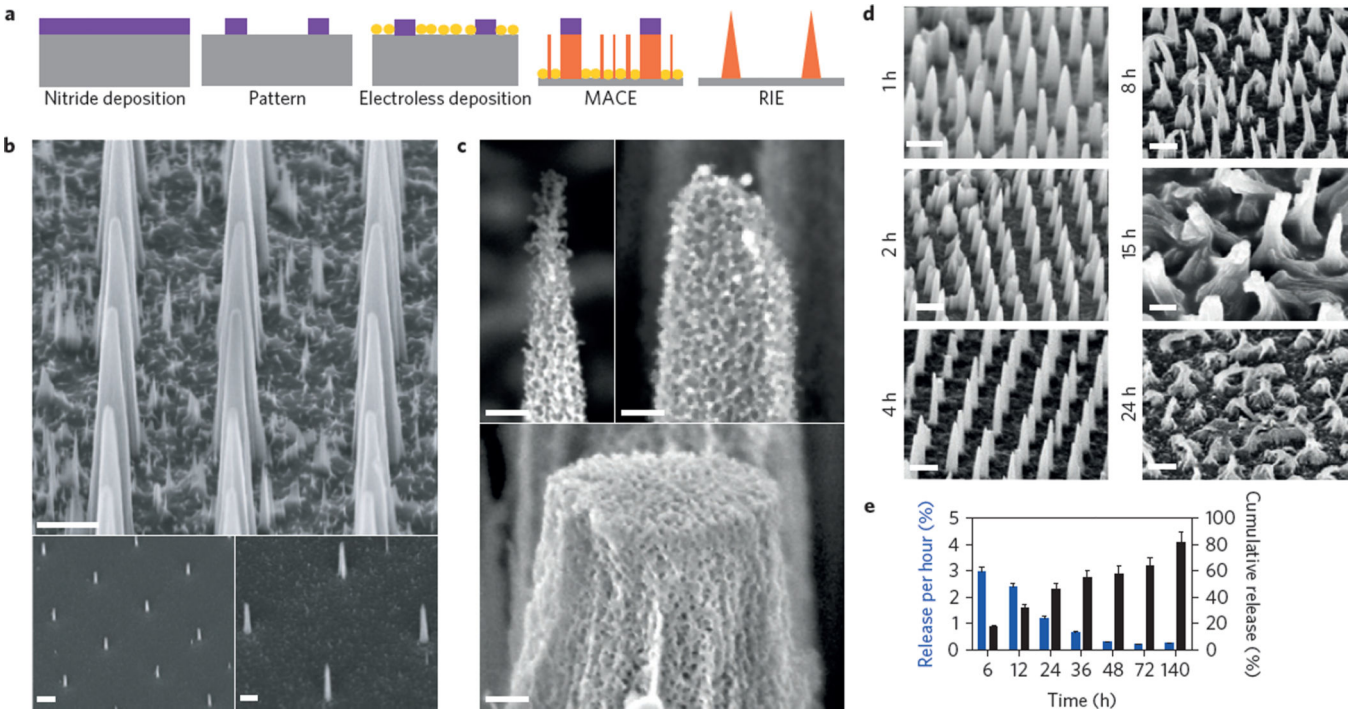


**Figure 1. Porous silicon nanoneedles**

**a**, Schematic of the nanoneedle synthesis combining conventional microfabrication and metal-assisted chemical etch (MACE). RIE, Reactive ion etching. **b,c**, SEM micrographs showing the morphology of porous silicon nanoneedles fabricated according to the process outlined in **a. b**, Ordered nanoneedle arrays with pitches of 2 μm, 10 μm and 20 μm, respectively. Scale bars, 2 μm. **c**, High-resolution SEM micrographs of nanoneedle tips showing the nanoneedles' porous structure and the tunability of tip diameter from less than 100nm to over 400 nm. Scale bars, 200 nm. **d**, Time course of nanoneedles incubated in cell-culture medium at 37 °C. Progressive biodegradation of the needles appears, with loss of structural integrity between 8 and 15 h. Complete degradation occurs at 72 h. Scale bars, 2 μm. **e**, ICP-AES quantification of Si released in solution. Blue and black bars represent the rate of silicon release per hour and the cumulative release of silicon, respectively, at each timepoint, expressed as a percentage of total silicon released. Error bars represent the s.d. of 3–6 replicates.

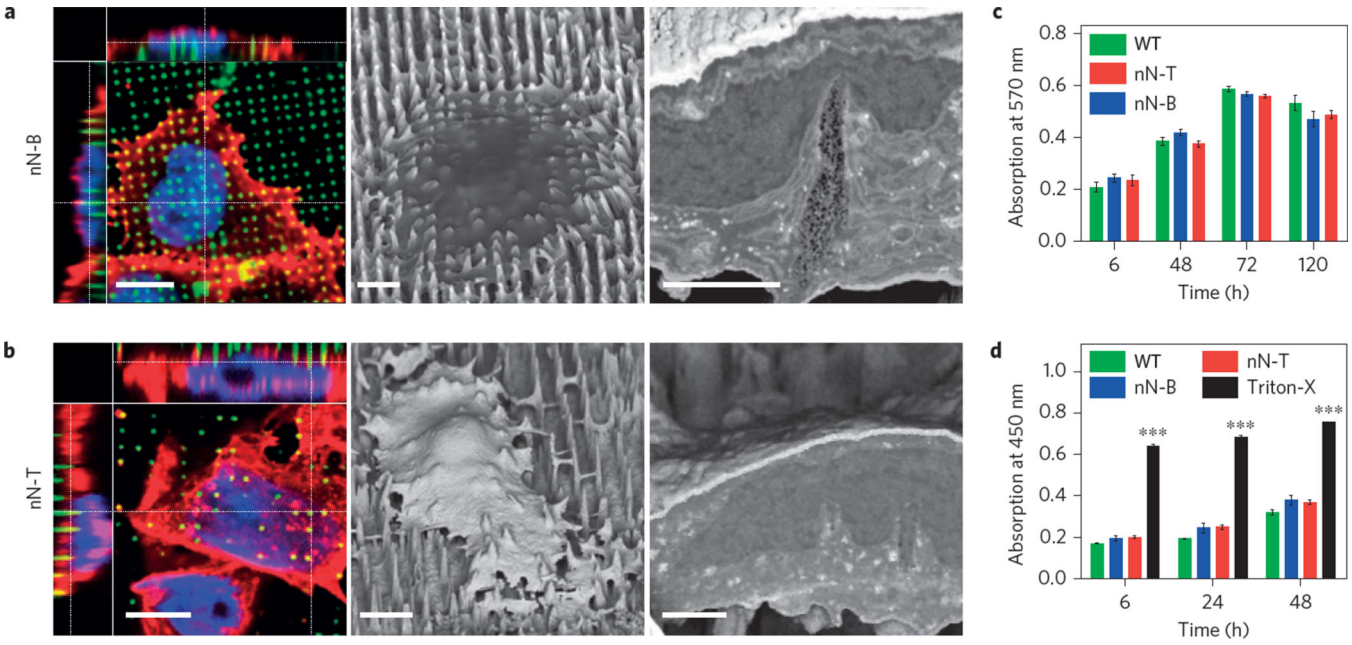


**Figure 2. Cell interfacing, cytocompatibility and biodegradation**

**a,b**, Confocal microscopy, SEM and FIB-SEM cross-sections of cells over nanoneedles (nN-B) at 4 h (**a**) and of nanoneedles on top of cells (nN-T; 100 rcf) at 0 h (**b**) show cell spreading, adhesion and nanoneedle interfacing. Scale bars, 10 μm confocal; 5 μm SEM; 2 μm FIB-SEM. **c**,MTT assay comparing the metabolic activity of cells grown on a flat silicon substrate (WT) with the activities for the nN-T and nN-B settings over the course of five days. **d**, LDH assay comparing the release of lactate dehydrogenase over the course of two days for human dermal fibroblasts (HDF) grown on nN-T, nN-B, and tissue culture plastic (WT). Cells incubated with Triton-X serve as positive controls for membrane permeabilization. ***$p$<0.001. Error bars in **c,d** represent the s.d. of 3 replicates.

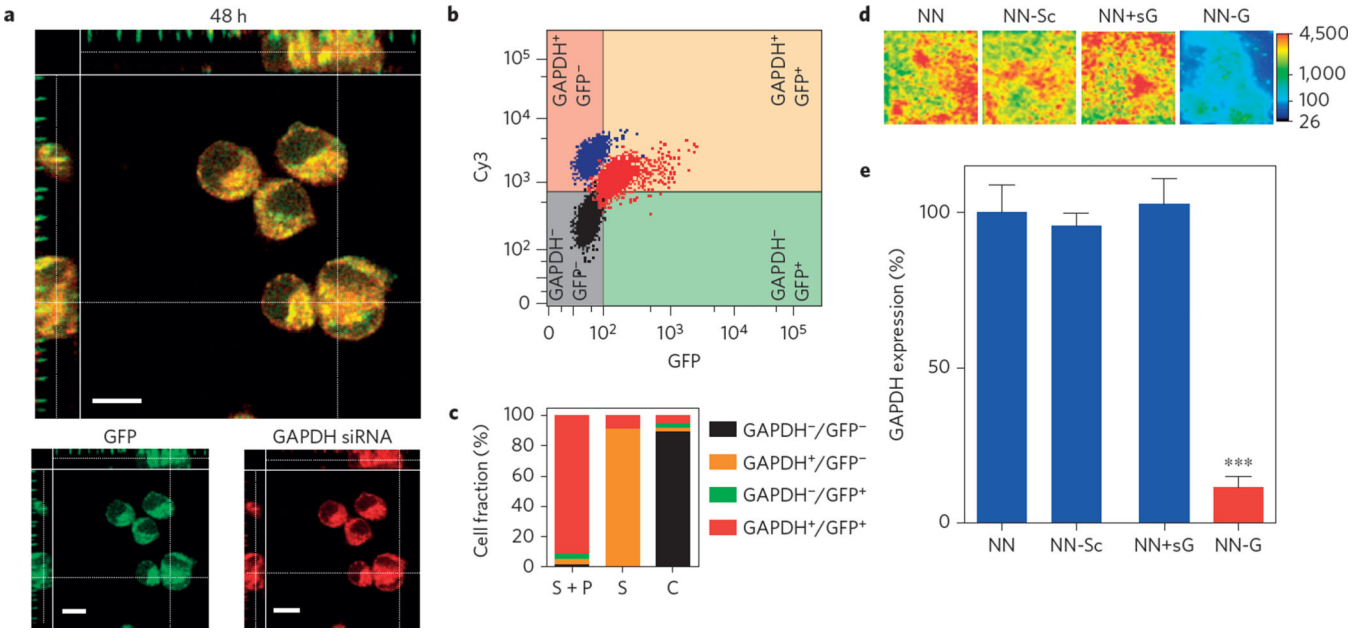


**Figure 3. Intracellular co-delivery of nucleic acids**

**a**, Co-delivery of GAPDH-siRNA (Cy3 labelled in yellow) and GFP plasmid (GFP in green) to cells in culture after application using the nN-B interfacing strategy. Confocal image acquired 48 h post transfection. The siRNA and GFP signal are present diffusely throughout the cytosol. Scale bars, 5 μm. **b**, Flow-cytometry scatter (dot) plot shows that >90% of siRNA transfected cells are positive for Cy3 (blue cluster) and that greater than 90% of co-transfected cells are positive for GFP and Cy3 (red cluster) compared with cells transfected with empty needles (black). **c**, Quantification of flow-cytometry data according to the gate outlined in **b** to show the percentage of GAPDH-positive, GFP-positive and double-positive cells for nanoneedles loaded with siRNA (S), siRNA and GFP plasmid (SCP). Empty needles were used as the control (C). **d**, In-cell western assay showing an entire nN-B chip seeded with cells. The fluorescent signal from GAPDH is significantly reduced for cells to which GAPDH siRNA has been delivered (NN-G) relative to empty nanoneedles (NN), nanoneedles loaded with scrambled siRNA (NN-Sc), and empty nanoneedles with GAPDH siRNA delivered from solution (NNCsG). **e**, Quantification of the in-cell western assay, showing statistically significant silencing of GAPDH expression to <20% of basal level only in cells treated with nanoneedles loaded with GAPDH. Basal level was evaluated for cells grown on empty nanoneedles. ***$p$<0.001. Error bars represent the s.d. of 3 replicates.

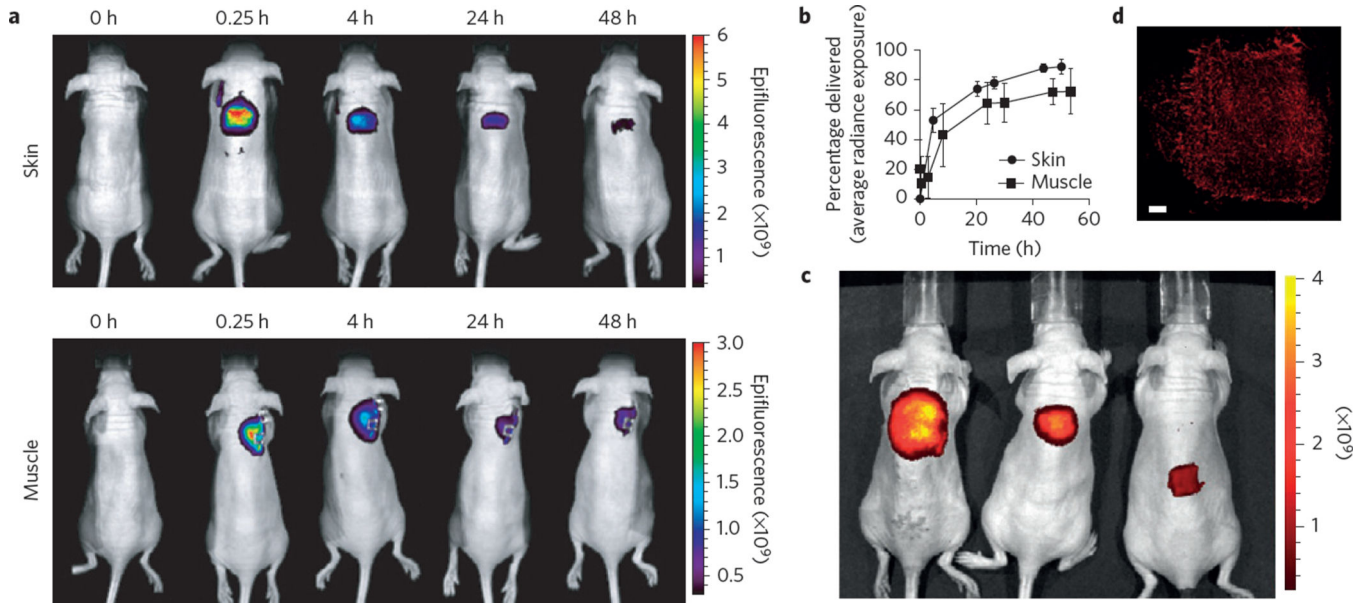


**Figure 4. Nanoneedles mediate *in vivo*** delivery. **a**, Longitudinal imaging of mice treated with nanoneedles on top of the skin or underneath the skin on the back muscle and loaded with a near-infrared fluorescent dye. The distribution and diffusion of the delivered fluorescent dye was monitored using whole-animal fluorescent imaging for 48 h. **b**, The delivery and diffusion of the dye was measured at several times following 1-min nanoinjection, and plotted to compare delivery kinetics at the different sites of administration. Error bars represent the s.d. of 3 replicates. **c**, Near-infrared fluorescent imaging on the skin of mice, comparing the delivery of DyLight 800 using a drop (left), flat Si wafer (middle), or nanoneedles (right). **d**, Intravital confocal image, showing the delivery pattern of dye-loaded nanoneedles. Scale bar, 1 mm.

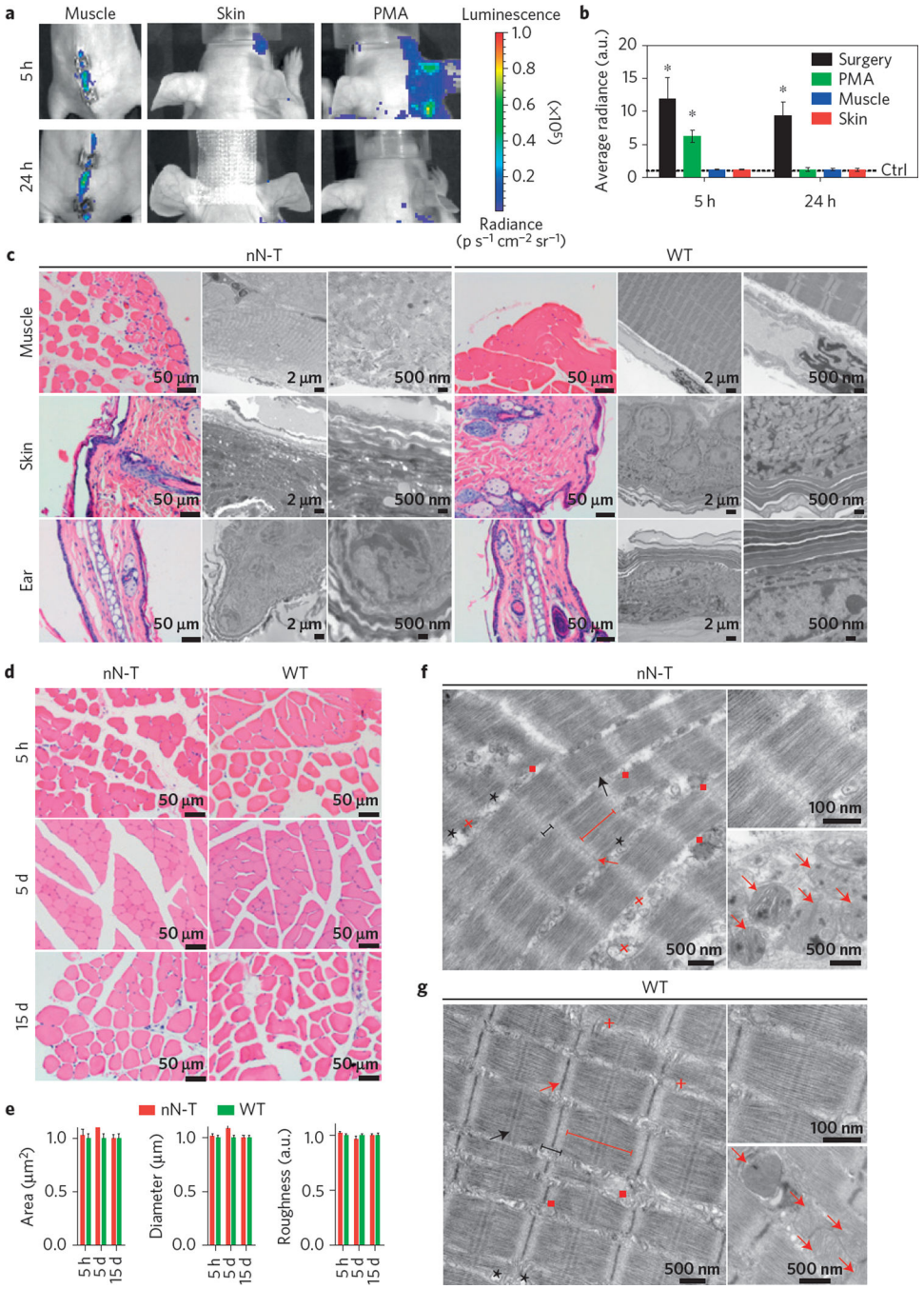


**Figure 5. Safety profile of nanoinjection**

**a**, Representative longitudinal bioluminescence images of mice with luminol at 5 and 24 h following nanoneedle treatment to the muscle and skin on the ear. Phorbol-12-myristate-13-acetate (PMA) treatment and surgical incisions were employed as positive controls. **b**, Quantification of the average radiance exposure acquired from mice administered with luminol at 5 and 24 h for surgical incision (black), PMA-treated ears (green), muscles (blue) and skin of ear (red) following treatment with nanoneedles. Data normalized to control represented by the black dashed line. *$p$<0.05 versus control. Error bars represent the s.d. of

3 replicates. **c**, H&E and TEM micrographs at the site of nanoinjection for muscle, skin and ear, comparing nanoneedles and control tissues. **d**, H&E images of muscle sections at 5 h, 5 days and 15 days following nanoinjection compared against wild-type (WT; that is, control) tissues. **e**, Quantification of individual myofibres for area, diameter and roughness for the times depicted in **d**. Error bars represent the s.d. of measurements in 34–92 areas (for nN-T: 49, 34 and 92 for 5 h, 5 d and 15 d, respectively; for WT: 60, 90 and 53 for 5 h, 5 d and 15 d, respectively) taken from 3 animals. **f,g**, TEM micrographs of muscle sections for nanoneedles (**f**) and control (**g**) sections, illustrating the impact of nanoinjection on the ultrastructure of tissues at low magnification. Higher-magnification images to the right depict intact myofibrils (top) and mitochondria (bottom). Red lines, A-band; black lines, I-band; black arrows, M-line; red arrows, Z-line; red crosses, transverse tubules; black stars, sarcoplasmic reticulum; red squares (or red arrows in high-magnification images), mitochondria.

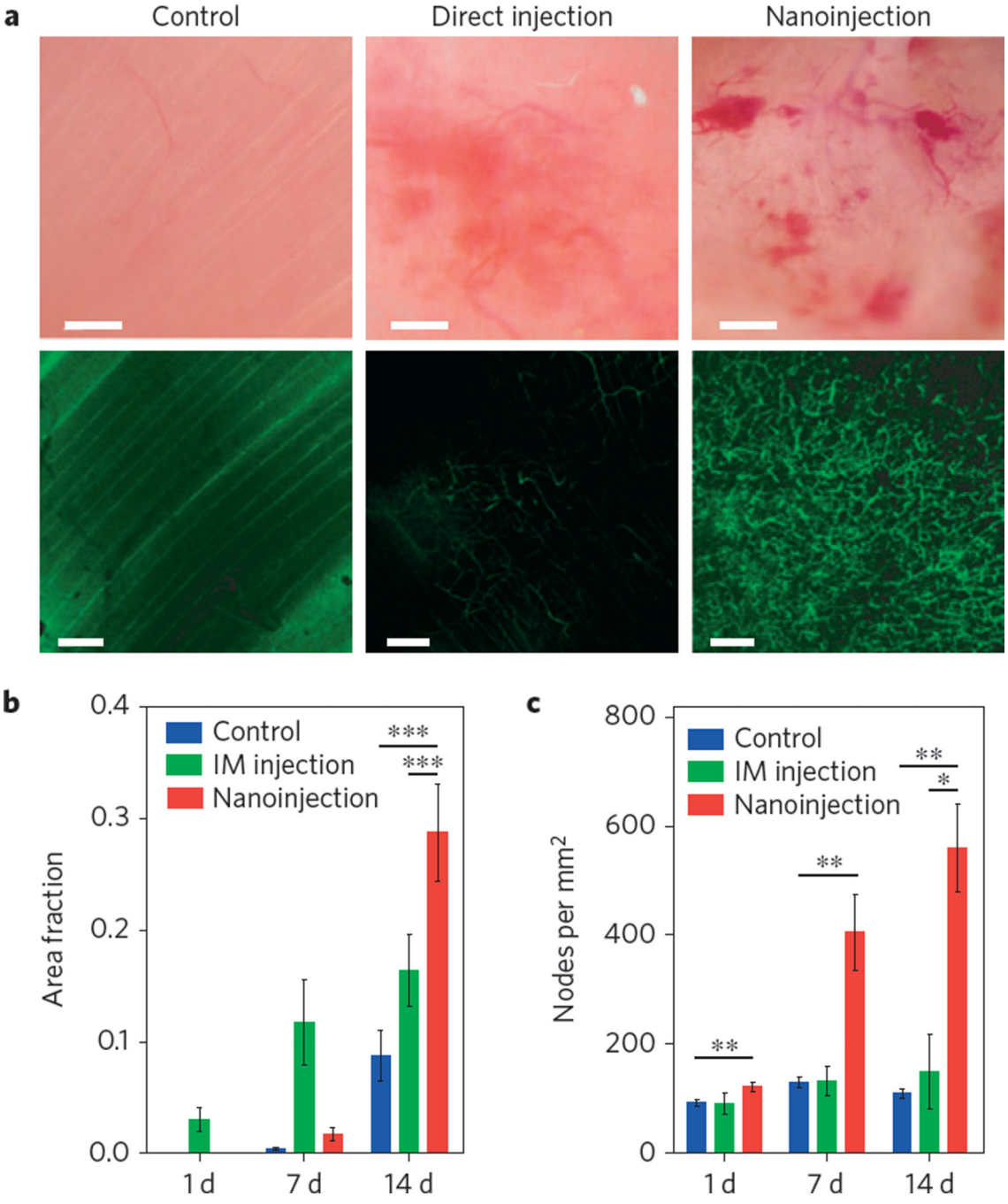


**Figure 6. Nanoneedles mediate neovascularization**

**a**, Intravital bright-field (top) and confocal (bottom) microscopy images of the vasculature of untreated (left) and hVEGF-165-treated muscles with either direct injection (centre) or nanoinjection (right). The fluorescence signal originates from systemically injected FITC–dextran. Scale bars, bright-field 100 μm; confocal 50 μm. **b,c**, Quantification of the fraction of fluorescent signal (dextran) (**b**) and the number of nodes in the vasculature per $mm^2$ (**c**) within each field of view acquired for untreated control, intramuscular injection (IM) and

nanoinjection. *$p$=0.05, **$p$<0.01, ***$p$<0.001. Error bars represent the s.d. of the averages of 5 areas taken from 3 animals.